MODIS/ASTER (MASTER) Airbone simulator

Level 3 Surface Mineralogy Algorithm Theoretical Basis Document (ATBD)

Version 0.1
November 11, 2025

[1]Federico Rabuffi, [1,2]Michael S. Ramsey, [3]James O. Thompson, [1]Glynn Hulley, [1]Simon J. Hook

MASTER Algorithm Development Team

[1]NASA-Jet Propulsion Laboratory, California Institute of Technology
[2]University of Pittsburgh
[3]University of Texas, Austin

National Aeronautics and Space Administration
Jet Propulsion Laboratory
California Institute of Technology

Jet Propulsion Laboratory
4800 Oak Grove Drive
Pasadena, California 91109-8099
California Institute of Technology

This research was carried out at the Jet Propulsion Laboratory, California Institute of Technology, under a contract with the National Aeronautics and Space Administration.

Change History Log

Revision	Effective Date	Prepared by	Description of Changes
Draft	11/10/2025	Federico Rabuffi	First draft

1 Contacts

Readers seeking additional information about this study may contact the following:

Federico Rabuffi
NASA – Jet Propulsion Laboratory, California Institute of Technology
4800 Oak Grove Drive, Room 183-5906B
Pasadena, California 91109-8099
Email: federico.rabuffi@jpl.nasa.gov
Office: 1-818-354-0854

Michael S. Ramsey
University of Pittsburgh
4107 O'Hara Street, Room 509
Pittsburgh, PA 15260-3332
Email: mramsey@pitt.edu
Office: 1-412-624-8772

James O. Thompson
University of Texas, Austin
10611 Exploration Way
Austin, TX 78758
Email: james.thompson@beg.utexas.edu
Office: 1-512-471-6775

Glynn Hulley
NASA – Jet Propulsion Laboratory, California Institute of Technology
4800 Oak Grove Drive
Pasadena, California 91109-8099
Email: glynn.hulley@jpl.nasa.gov
Office: 1-818-354-2979

Simon J. Hook
NASA – Jet Propulsion Laboratory, California Institute of Technology
4800 Oak Grove Drive
Pasadena, California 91109-8099
Email: simon.j.hook@jpl.nasa.gov
Office: 1-818-354-0974

2 Abstract

The MODIS/ASTER Airborne Simulator was developed for the Advanced Spaceborne Thermal Emission and Reflection Radiometer (ASTER) and Moderate Resolution Imaging Spectroradiometer (MODIS) projects. ASTER and MODIS are two spaceborne imagining instruments launched in the fall of 1999 hosted on Terra platform. ASTER provides high spatial resolution observations with 15 m in the VNIR, 30 m in the SWIR and 90 m in the TIR across a total of 14 spectral channels, spanning approximately 0.5 to 12 micron. The swath is 60 km, and it achieves nominal 16 day repeat coverage. ASTER has also along-track stereo imaging, enabling detailed topographic and local-scale studies using visible through thermal infrared data.

MODIS provides moderate-to-coarse resolution observations of 250 m (2 channels), 500 m (5 channels) and 1 km (29 channels) covering a spectral range from 0.4 to 14 micron. Its swath width is 2330 km, providing near-daily global coverage (with the except near the equator).

The primary mission of MASTER was to collect ASTER-like and MODIS-like data, at higher spatial resolution, to provide an additional radiometric calibration and to support validation of the ASTER and MODIS geophysical retrieval algorithms and permit scaling studies and comparison with in-situ measurements.

Beyond his primary objectives, over the years, MASTER has continued to operate, evolving into the Geological Earth Mapping Experiment (GEMx) – a joint campaign between NASA and the U.S. Geological Survey (USGS). GEMx is designed to map portions of the southwest United States for critical minerals using advanced airborne imaging. In addition to that, MASTER serves as a key platform for generating simulated data in support of future thermal infrared missions, as the Surface Biology and Geology – Thermal Infrared (SBG-TIR), Thermal Infrared Imaging Satellite for High-resolution Natural resource Assessment (TRISHNA), Landsat Next, and Land Surface Temperature Monitoring (LSTM).

This document describes the Level-3 Surface Mineralogy products.

Contents

Figures

Tables

3 Introduction

The MODIS/ASTER (MASTER) airborne simulator is a multispectral scanning instrument that acquires data across the 0.4-to-13-micron spectral window using 50 channels spanning in visible (VIS), near infrared (NIR), shortwave infrared (SWIR), mid infrared (MIR) and thermal infrared (TIR). Depending on the aircraft altitude, the spatial resolution provided by MASTER can vary between approximately 5 to 50 m, with an 85.9° total field of view and a variable swath width determined by the aircraft platform (DOE B200, NASA ER-2, or NASA DC-8). A comparison with spaceborne thermal sensors in orbit and planned, is reported in Table 1.

Table 1: MASTER measurement characteristics compared to other operational and planned (*) spaceborne TIR instruments

Instrument	**Platform**	**Resolution (m)**	**Revisit (days)**	**Daytime overpass**	**TIR bands (8-12.5 µm)**	**Launch year**
MASTER	**Aircraft: B200; ER-2; DC-8**	**~ 5 to 50 (altitude dependent)**	**Airborne campaign-based**	**Yes – campaign based**	**10**	**1st campaign 1998-1999**
OTTER	SBG	60	3	12:30	6	2028*
ECOSTRESS	ISS	38 × 68	3-5	Variable	5	2018
LSTM		50	4	13:00	5	2028*
TRISHNA		57	2-3	13:00	4	2025*
ASTER	Terra	90	16	10:30	5	1999
ETM+/TIRS	Landsat 7/8	60-100	16	10:11	1/2	1999/2013
VIIRS	Suomi-NPP	750	Daily	1:30 / 13:30	4	2011
MODIS	Terra/Aqua	1000	Daily	10:30 / 13:30	3	1999/2002
GOES	Multiple	4000	Daily	Every 15 min	2	2000

This document outlines the theory and methodology for generating the MASTER Level-3 (L3) Surface Mineralogy (SM) product. The MASTER L3 SM product uses the Level-2 (L2) TIR surface emissivity data as input together with a spectral library of the most common Earth surface minerals acquired in emission in the laboratory at 2 cm^{-1} resolution (Christensen et al., 2000). Most silicates, carbonates, and other rock-forming minerals have diagnostic spectral features in the TIR regions characterized by the strongest absorption bands also known as Reststrahlen features (Figure 1).

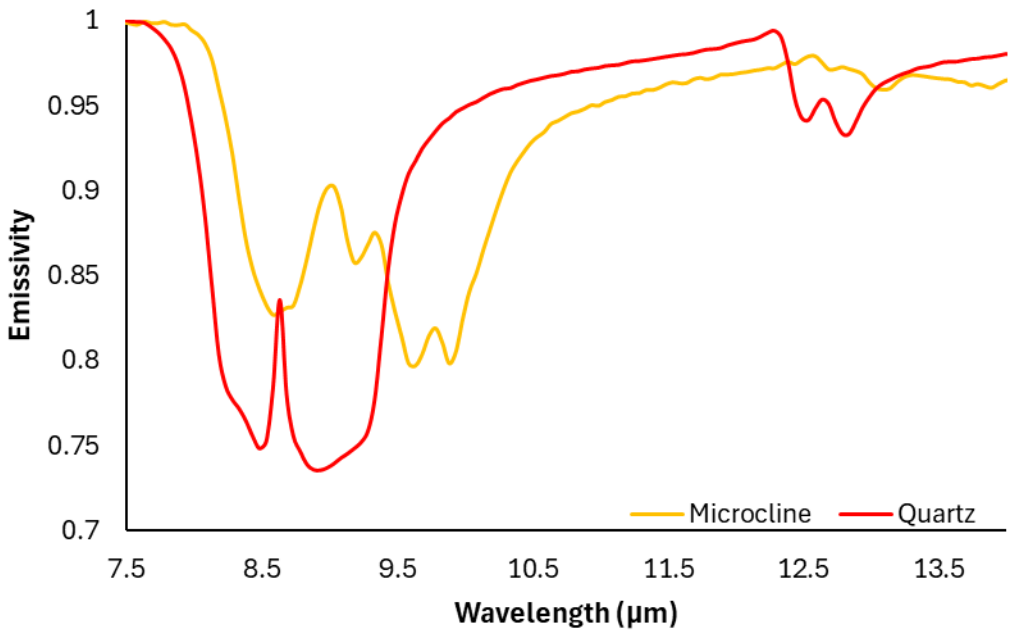

Figure 1: TIR (8.0 – 13.0 µm) spectral emissivity of quartz and microcline (potassium feldspar) showing the diagnostic Reststrahlen emissivity features for both minerals. Data from: ASU Spectral Library (Christensen et al., 2000).

The SM algorithm used to generate MASTER L3 SM reflects the SM code developed for the SBG-TIR Level-3 Surface Mineralogy Products (Ramsey et al., 2024, Ramsey et al., 2025, Rabuffi et al., 2025). A spectral comparison between SBG-TIR and MASTER will be presented

in Section 4.3 to more clearly justify the applicability of the same methodology and the validity of the corresponding validation procedures.

The SM code uses the principal of linear spectral mixing in TIR region where the larger absorption coefficients typical of most rock-forming minerals limit photon transmission and scattering within the mineral grains. The emitted spectrum, therefore, has spectral features in linear proportion to the areal abundance of those minerals in the unknown sample (Ramsey and Christensen, 1998). In contrast, this scattering is more prevalent in the visible short-wave infrared (VSWIR) causing non-linearity in the reflectance spectrum and requiring more complex mapping approaches to mineral identification (Clark et al., 2003, Connelly et al., 2021).

The SM code is applied to the at-surface TIR emissivity data derived from the MASTER L2 dataset. It will be applied to all datasets, regardless of the acquisition area, and to all pixels with an MMD emissivity value greater than 0.02. On these bases, results obtained over urban areas, vegetated surfaces, water bodies or cloudy scenes are not representative of the general outcome and should be interpreted with caution. The emission spectrum from any pixel meeting the MMD criteria is modeled using the pre-determined spectral library as input and producing a best-fit suite of mineral endmember images plus their corresponding residual error images. A root-mean-squared (RMS) error image is also produced to assess the overall goodness-of-fit of the model. Finally, a weight percent silica (WPS) image is also produced using the approach of Hook et al. (2005), based on the spectral shift of the diagnostic Si-O spectral feature.

The remainder of the document will discuss the MASTER instrument characteristics, provide a background on TIR remote sensing, give a full description and background on the SM algorithm.

4 MASTER - Instrument Characteristics

4.1 Radiometer

As described in Hook et al., (2001) - The MASTER instrument was developed by the NASA Ames Research Center in conjunction with the Jet Propulsion Laboratory. It consists of three key components: a scanning spectrometer, a digitizer, and a data storage system. The scanning unit was built by Sensys Technology (formerly Daedalus Enterprises), while the digitizer and data storage system was a collaborative effort between Berkeley Camera Engineering and the Ames Airborne Sensor Facility (ASF), which also managed the system integration

MASTER supports a variety of scan speeds, allowing the acquisition of contiguous imagery from different altitudes and with varying pixel sizes (Table 2). The optical system includes a spectrometer mounted on a scanning fore-optic unit. Both the spectrometer and fore-optics portions are mated to an optical baseplate. The fore-optics employ a 45° rotating scan mirror that directs light into a Gregorian telescope, through a series of mirrors and apertures, and finally into the spectrometer.

The spectrometer separates incoming radiation into four wavelength regions – VIR, SWIR, MIR and TIR – using dichroic beam slitters. Each region is dispersed by a diffraction grating onto its own detector array. The system design ensures high optical efficiency and radiometric uniformity across the field of view. Electrical signals from the detectors are amplified, digitized through adaptive 16-bit converters, and stored along with navigation and engineering data. The use of actively controlled preamplifiers and optical isolation minimizes noise and calibration drift, ensuring high radiometric accuracy. Further details of the optical system are given in King et al. (1996).

Table 2: MASTER sensor - Summary Characteristics

Summary characteristics	
Wavelength Range (µm)	0.4 - 13
Number of channels	50
Number of pixels	716
Instantaneous field of view	85.92°
Platforms	DOE King Air Beachcraft B200; NASA ER-2; NASA DC-8
Pixel size DC-8 (m)	10 – 30
Pixel size NASA ER-2 (m)	50
Pixel size DOE King Air Beachcraft B200 (m)	5 – 25
DC-8 range – without refueling	5403 statute miles
ER-2 range – without refueling	3700 statute miles
B200 range – without refueling	700 statute miles
Scan speed	6.25/12/5/25 rps
Calibration VIS-SWIR	Laboratory Integrating Sphere
Calibration MIR-TIR	2 on-board blackbodies
Data Format	Hierarchical Data Format (HDF)
Digitalization	16-bit
Products	
Level 1B	Radiance at sensor
Level 2	Emissivity and Land Surface Temperature
Level 3	Surface Mineralogy Analysis
	Evapotranspiration
	Elevated Temperature Feature
	Fire Radiative Power

4.2 Band positions

MASTER - airborne sensor - acquires multispectral data across the VSWIR to TIR region using 50 channels ranging from 0.4 to 13 microns. The spectral configuration, listed in Table 3, is divided into 4 regions: VNIR (channels 1-11); SWIR (channels 12-25); MIR (channels 26-40); TIR (channels: 41-50). The TIR includes channels in the wavelength range: 7.7-12.9 micron, providing continuous coverage of the atmospheric window and enabling detailed analysis of surface thermal properties. The center wavelength position and width of each band – width-at-half-maximum (FWHM) – are defined by the geometry of the grating-based spectrometer and are calibrated before and after each major flight campaign. Therefore, small shift in channel center positions may occur between calibration cycles and the calibration closest to the acquisition date should be used when performing quantitative spectral analyses.

In the current MASTER Thermal and Emissivity Separation (TES) algorithm, only atmospheric window bands are used to retrieve spectral emissivity and the land surface temperature. These include band 43 (8.61 μm), 44 (9.05 μm), 47 (10.62 μm), 48 (11. 31μm), and 49 (12.11 μm) – see Figure 2. MASTER Band 42 (8.18 μm) falls within the strong water absorption band located at 6.3 μm (ν_2 bending mode) where atmospheric transmittivities can decrease below 60% for high water vapor conditions. MASTER band 50 (12.84 μm) falls within the water vapor rotation band that extends beyond 12 μm and is also not included in TES for that reason. Currently we do not have the necessary accuracy, nor spatial resolution in water vapor profiles used to atmospherically correct thermal infrared data for these two bands, that could result in large uncertainties in LST&E retrievals from TES exceeding 2 K in LST and 2.5% in emissivity. Similarly, MASTER band 45 (9.68 μm) and band 46 (10.08 μm) are not used in TES because they fall within the strong ozone (O_3) absorption centered around 9.6 μm (the ν_3 asymmetric stretch

vibration band). In this region atmospheric transmittances can range between 20-40% resulting in very little surface radiance reaching the sensor and resulting in large LST&E errors and noisy retrievals.

It is expected that small adjustments to the band positions, widths, and transmission will be made based on ongoing engineering filter performance capabilities and finalized once the filters are fabricated.

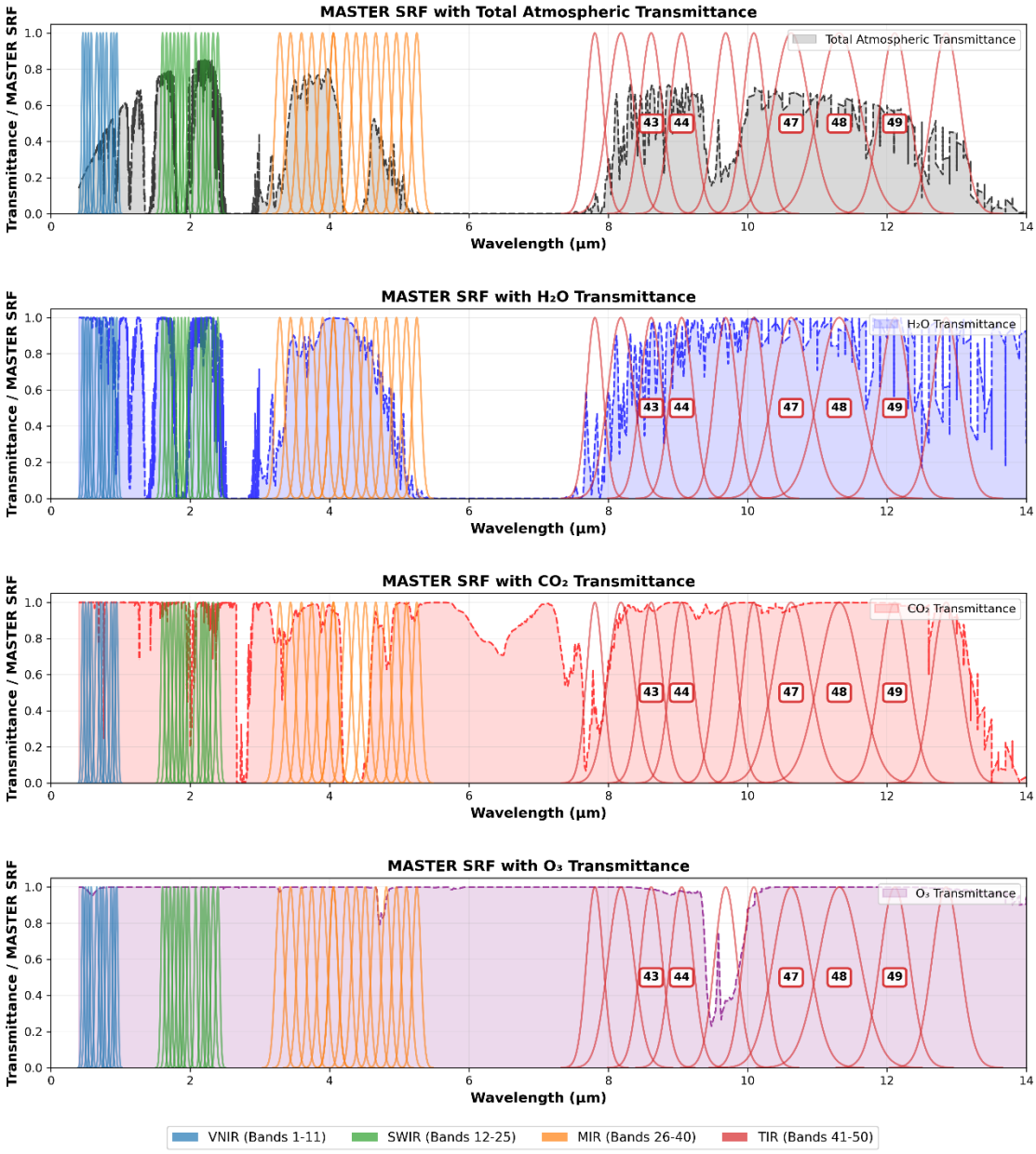

Figure 2: MASER Spectral Response Function (September 2025). 50 bands: 11 in the VNIR (light blue); 14 in the SWIR (green); 15 in the MIR (orange); and 10 in the TIR (red). MASTER SRF is plotted against the atmospheric transmittance. From the bottom: O3 transmittance (purple); CO2 transmittance (red); H2O transmittance (blue); total transmittance (grey).

Table 3: MASTER SRF based on the 2025 campaign - Date of Calibration: Sep 2025; location: NASA Aims. More details at: https://asapdata.arc.nasa.gov/sensors/master/data/srf/Sep_25_srf.html

(μm)	Band#	Full width half maximum	Channel Center	Channel peak
VNIR – 1	1	0.0412	0.4596	0.46
VNIR – 2	2	0.0451	0.4984	0.5
VNIR – 3	3	0.0431	0.5409	0.542
VNIR – 4	4	0.0412	0.5804	0.58
VNIR – 5	5	0.0598	0.6602	0.652
VNIR – 6	6	0.0412	0.7101	0.71
VNIR – 7	7	0.0405	0.7495	0.75
VNIR – 8	8	0.0406	0.7991	0.8
VNIR – 9	9	0.0412	0.8651	0.866
VNIR – 10	10	0.0408	0.9053	0.906
VNIR – 11	11	0.0418	0.946	0.946
SWIR – 1	12	0.056	1.6037	1.604
SWIR – 2	13	0.055	1.6605	1.66
SWIR – 3	14	0.0516	1.7153	1.716
SWIR – 4	15	0.0526	1.7696	1.77
SWIR – 5	16	0.0479	1.8249	1.83
SWIR – 6	17	0.04	1.8744	1.876
SWIR – 7	18	0.0504	1.927	1.928
SWIR – 8	19	0.0476	1.9764	1.978

SWIR – 9	20	0.0479	2.0787	2.08
SWIR – 10	21	0.0468	2.1605	2.162
SWIR – 11	22	0.0485	2.2107	2.212
SWIR – 12	23	0.0473	2.2604	2.262
SWIR – 13	24	0.0701	2.3298	2.32
SWIR – 14	25	0.0632	2.3961	2.39
MIR – 1	26	0.1457	4.0552	4.065
MIR – 2	27	0.144	3.2864	3.295
MIR – 3	28	0.1486	3.4405	3.455
MIR – 4	29	0.1479	3.5966	3.61
MIR – 5	30	0.135	3.7432	3.76
MIR – 6	31	0.1534	3.9009	3.915
MIR – 7	32	0.1457	4.0552	4.065
MIR – 8	33	0.153	4.2472	4.2426
MIR – 9	34	0.153	4.3812	4.3766
MIR – 10	35	0.1412	4.5119	4.52
MIR – 11	36	0.1481	4.6633	4.68
MIR – 12	37	0.1477	4.8149	4.83
MIR – 13	38	0.1402	4.9601	4.98
MIR – 14	39	0.1434	5.1038	5.105
MIR – 15	40	0.1376	5.2518	5.26
TIR – 1	41	0.2805	7.8069	7.83

TIR – 2	42	0.4333	8.1814	8.25
TIR – 3	43	0.3683	8.6155	8.65
TIR – 4	44	0.3837	9.0527	9.05
TIR – 5	45	0.377	9.6853	9.71
TIR – 6	46	0.3745	10.0892	10.11
TIR – 7	47	0.6101	10.6241	10.58
TIR – 8	48	0.6973	11.3144	11.17
TIR – 9	49	0.4929	12.1104	12.06
TIR – 10	50	0.4754	12.8487	12.81

4.3 Comparison with SBG-TIR (Surface Biology and Geology – Thermal Infrared)

This section presents a spectral comparison between SBG-TIR and MASTER to analyze their level of compatibility for mineralogical applications. This will include the study of the band positions, widths and overall spectral coverage. This comparative analysis allows to assess how close the two sensors align, supporting the reliability of transferring the methodology and validation procedures developed for SBG-TIR to MASTER.

The spectral comparison between SBG-TIR and MASTER reveals a high degree of correspondence in band positioning within the TIR region. The two sensors share the same six-band configuration covering the 8-12 μm atmospheric window. MASTER bands 42-44 and 47-49 align closely with SBG-TIR channels: band 42 (center: 8.18 μm) corresponds to TIR-1 (8.32 μm) with a deviation of 0.14 μm; band 43 (8.62 μm) matches TIR-2 (8.63 μm) within 0.01 μm; band 44 (9.05 μm) aligns with TIR-3 (9.07 μm) with 0.02 μm difference; band 47 (10.62 μm) relates to TIR-4 (10.30 μm) showing the largest offset of 0.32 μm; band 48 (11.31 μm) corresponds to TIR-5 (11.35 μm) with 0.04 μm deviation; and band 49 (12.11 μm) aligns with TIR-6 (12.05 μm) within 0.06 μm.

Four of the six band pairs show very close spectral alignment, while slight differences occur in two cases. MASTER band 47 (10.62 μm) shows a 0.32 μm offset from SBG TIR-4 (10.30 μm), representing the largest wavelength deviation between the two sensors. Additionally, MASTER band 42 exhibits an offset from SBG TIR-1; however, as specified in Section 4.2, band 42 is not used to retrieve MASTER Level-2 emissivity product. Instead, band 42 is replaced by an emissivity band centered at 8.3 μm, generated from the Advanced Spaceborne Thermal Emission and Reflection Radiometer (ASTER) emissivity band 10 and 11. This process in the MASTER

L2 emissivity data mitigates the apparent discrepancy observed at the sensor level, bringing the operational band centers into closer alignment for practical applications.

Overall, despite some variation in terms of bandwidth, the sensors can be considered spectrally comparable with respect to the algorithm's applicability to mineralogical applications.

Nevertheless, MASTER data were in fact chosen to simulate SBG-TIR data (Ramsey et al., 2024, Ramsey et al., 2025, Rabuffi et al., 2025)

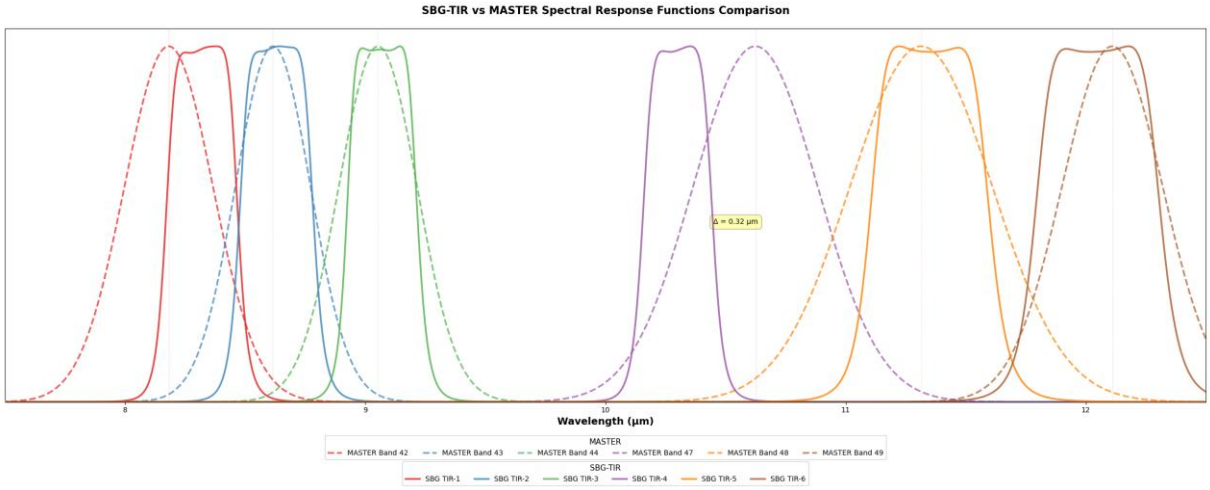

Figure 3: Spectral comparison in the TIR between the SBG-TIR sensor and MASTER.

5 Theory

5.1 Mid-wave and Thermal Infrared Remote Sensing Background

The at-sensor measured radiance in the infrared region (3–13 μm) consists of a combination of different terms from surface emission, solar reflection, and atmospheric emission and attenuation. The Earth-emitted radiance is a function of the temperature and emissivity of the surface, which is then attenuated by the atmosphere on its path to the satellite. The emissivity of an isothermal, homogeneous emitter is defined as the ratio of the actual emitted radiance to the radiance emitted from a blackbody (Figure 1) at the same thermodynamic temperature (Norman and Becker 1995), $\epsilon_\lambda = R_\lambda / B_\lambda$. Emissivity is an intrinsic property of the surface material and is an independent measurement from the surface temperature, which varies with irradiance, local atmospheric conditions, time of day, and specific conditions causing elevated temperature (e.g., wildfires, volcanic eruptions, etc.). The emissivity of most natural Earth surfaces varies from ~0.7 to close to 1.0, for the TIR wavelength (8–13 μm) for spatial scales <100 m. Narrowband emissivities less than 0.85 are typical for most desert and semi-arid areas due to the strong quartz absorption feature (Reststrahlen band) between the 8.0 and 9.5 μm, whereas the emissivity of green vegetation and water are generally greater than 0.95 and spectrally flat in the TIR. Dry and senesced vegetation as well as ice and snow can have lower emissivity values in the wavelengths longer than 10 μm.

The atmosphere also emits TIR radiation, a percentage of which reaches the sensor directly as "path radiance," whereas some amount is radiated downward to the surface (irradiance) and reflected back to the sensor. This is commonly known as the reflected downwelling sky irradiance. One effect of the sky irradiance is the reduction of the spectral contrast of the emitted surface radiance, due to Kirchhoff's law. Assuming the spectral variation in emissivity is small

(Lambertian assumption) and using Kirchhoff's law to express the hemispherical-directional reflectance as directional emissivity (ρ_λ=1-ϵ_λ), the at-sensor measured radiance in the infrared spectral region is a combination of three primary terms: the Earth-emitted radiance, reflected downwelling radiance (thermal + solar components), and total atmospheric path radiance (thermal + solar components).

$$L_{obs}(\lambda,\theta) = \tau_\lambda(\theta)\left[\epsilon_\lambda B(\lambda,T_s) + \rho_\lambda\left(L_s^{\downarrow}(\lambda,\theta) + L_t^{\downarrow}(\lambda,\theta)\right)\right] + L_t^{\uparrow}(\lambda,\theta) + + L_s^{\uparrow}(\lambda,\theta) \qquad (1)$$

where: L(λ,θ) = at-sensor radiance, λ is wavelength, θ is the satellite viewing angle, ϵ_λ is the surface emissivity, ρ_λ is surface reflectance, B(λ,T_s) is the Planck function describing radiance emitted at surface temperature, T_s, $L_s^{\downarrow}$ is the total (diffuse and direct) downwelling solar radiance, $L_t^{\downarrow}$ is the downwelling thermal irradiance, τ_λ (θ) is the atmospheric transmittance, $L_s^{\uparrow}$ (λ,θ) is the upward path solar radiance, and $L_t^{\uparrow}$ (λ,θ) is the upward thermal path radiance reaching the sensor.

The Temperature Emissivity Separation (TES) Algorithm originally created for ASTER TIR (Gillespie et al., 1998) data will be used to derive surface temperature and emissivity from the MASTER radiance data. The algorithm combines and improves upon some core features from previous temperature emissivity separation algorithms. TES combines the normalized emissivity method (NEM), the ratio, and the minimum-maximum difference (MMD) algorithm to retrieve temperature and a full emissivity spectrum. The NEM algorithm is used to estimate temperature and iteratively remove the sky irradiance, from which an emissivity spectrum is calculated, and then ratioed to their mean value in the ratio algorithm. At this point, only the shape of the emissivity spectrum is preserved, but not the amplitude. In order to compute an accurate temperature, the correct amplitude is then found by relating the minimum emissivity to the spectral contrast (MMD). Once the correct emissivity values are found, a final temperature can be calculated with

the maximum emissivity value. Additional improvements involve a refinement of ϵ_{max} in the NEM module and refining the correction for sky irradiance using the ε_{min}-MMD final emissivity and temperature values. Numerical modeling studies showed that TES can recover temperatures to within 1.5 K and emissivity values to within 0.015 over most scenes, assuming well calibrated, accurate radiometric measurements with a minimum of noise (Gillespie et al. 1998).

5.2 Compositional Detection in the TIR

The emission spectra from laboratory samples or pixels in a TIR image that are comprised of more than one mineral reflect those mineral endmembers by a combination of their characteristic spectral features. Perhaps more importantly, under most circumstances, those features are a linear combination of the areal percentage of the mineral endmembers themselves (Figure 4). The assumption of linear mixing of thermal radiant energy is valid due to the fact that most geologically significant minerals have very high absorption coefficients in the TIR, resulting in a much shorter path length and less scattering for the emitted photons. As a result, the majority of the energy detected by a sensor has interacted with only one surface particle (Ramsey and Christensen, 1998).

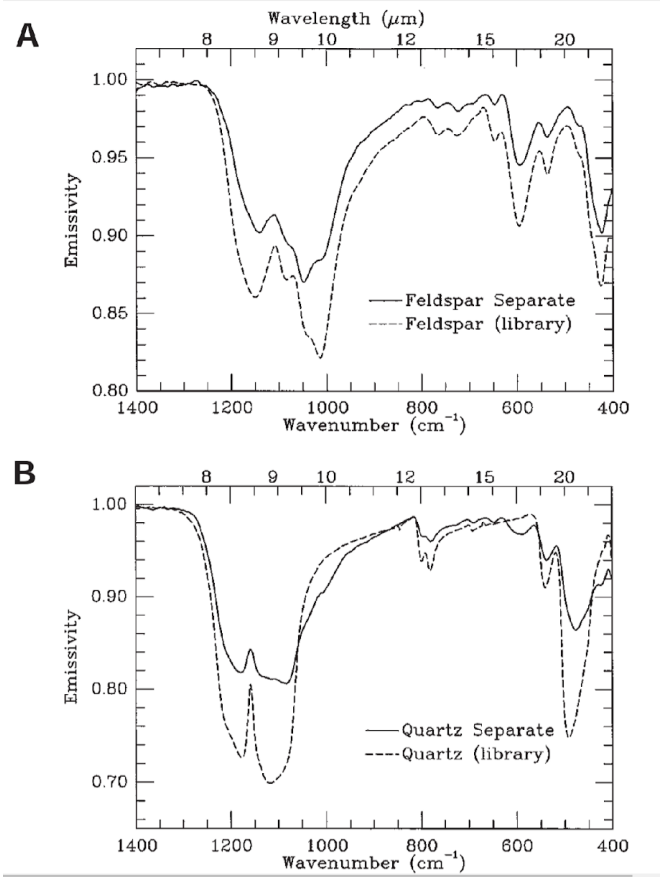

Figure 4: Emission spectra of the best-case separation of feldspar and quartz derived from the heavy-liquid technique. (A) Feldspar. (B) Quartz. Each spectrum is plotted with a pure library end member for comparison. From Ramsey and Christensen (1998).

Upon mixing, the spectral features from surface particles are retained in proportion to their areal extent. For example, Ramsey and Christensen (1998) showed this in spectra from Kelso Dunes, CA. The individual mineral grains in sand samples were separated using a heavy liquid technique, which proved to be only partially successful (Figure 4). Contamination of each spectrum by the other mineral is visible in the spectral features being most evident in the quartz spectrum, where 34% feldspar still remained. This contamination shows as a reduction in contrast of the primary absorption band at 1150 cm^{-1}, the development of band shoulder at 1000 cm^{-1}, and several smaller absorption bands between 600 cm^{-1} and 700 cm^{-1}.

3.1.1 Spectral Mixture Analysis (SMA)

This allows for a relatively straight forward approach to spectral analysis using some variation of linear spectral mixture analysis (Heinz 2001; Somers et al. 2011; Tompkins et al. 1997). This can be summarized by equation 2.

$$\varepsilon(\lambda)_{mix} = \sum_{i=1}^{\eta} (\zeta_i \cdot \varepsilon(\lambda)_i) + \delta(\lambda); \quad \langle 1 \rangle \quad \sum_{i=1}^{\eta} \zeta_i = 1.0; \quad \langle 2 \rangle \quad \zeta_i \geq 0 \qquad (2)$$

Where, η is the number of endmembers modeled, ζ_i is the areal fraction of the i^{th} endmember's emissivity ($\varepsilon(\lambda)_i$) and $\delta(\lambda)$ is the residual difference between the measured and modeled emissivity at wavelength (λ). The first constraint $\langle 1 \rangle$ placed upon the system is that the endmember fractions must sum to 1.0 (100%) per pixel for each model run. Because the equation is a relatively simple constrained, least-squares fit, negative endmember fractions are mathematically valid and occur in the rare cases where the spectrum of the unknown sample has a lower emissivity in some/all of the spectral range versus that of the endmember spectra. In these cases, the second constraint $\langle 2 \rangle$ is tested and negative endmembers removed from the modeling.

Therefore, assuming that the pure mineral spectra (i.e., the endmembers) are known, TIR spectra can be linearly deconvolved using the least-squares approach (equation 2) to ascertain the mineralogic percentages. For image-based analyses, this results in one image per endmember together with several checks on the accuracy of that model fit. A residual error image is produced for each TIR band, which is simply the measured – the modeled emissivity in that spectral band. Areas of high residual error indicate a poor model fit in that spectral band with the chosen endmembers. This difference is a critical measure of the retrieval algorithm's fit, and easily visualized where displayed versus wavelength, or as an image in the case of remotely gathered data (Gillespie et al., 1990). High residual errors at specific wavelengths indicate the possibility of an unmodeled absorption feature not present in either the endmember or mixture spectrum. An examination of residuals may also reveal nonlinear behavior at certain wavelengths as well as highlight areas of poor atmospheric correction and/or low instrument signal to noise (SNR).

A singular goodness-of-fit error image is also produced for each image/model run. The root-mean-squared (RMS) error image becomes invaluable in order to assess the overall quality of

a given algorithm iteration. For an instrument with (m) wavelength bands, the RMS is related to the per-band residual error (δ(λ)) using equation 3.

$$RMS = \sqrt{\frac{\left(\sum_{j=1}^{m} \delta(\lambda)_j^2\right)}{m}} \quad (3)$$

In the most common approach to spectral deconvolution, the number of endmembers modeled must be ≤ the number of spectral bands. Thus, for hyperspectral data, the number of possible endmembers can be quite high (to the point of being geologically implausible). However, for multispectral data, the limited number of spectral bands commonly places a tight constraint on the number of endmembers. This constraint may be acceptable if one is modeling the highest percentage two or three mineral endmembers using five or six band TIR data. If more than five or six endmember are present (or if one wants to test for the presence of many unknown minerals), a different approach is required such as the Multiple Endmember SMA (MESMA), which uses a combinatorial approach to testing all possible endmember combinations for the one producing the best fit (e.g., the lowest RMS error).

3.1.2 Multiple Endmember SMA (MESMA)

Linear SMA assumes that a mixed spectrum can be modeled as a linear combination of pure spectra, known as endmembers (Adams et al., 1986; Ramsey and Christensen, 1998). Under ideal conditions, the most accurate fractional estimates can be achieved using the minimum number of endmembers required to account for spectral variability within a mixed pixel (Sabol et al. 1992). Fractional errors occur either where too few endmembers are used, resulting in spectral information not modeled by the existing endmembers; or too many, resulting in incorrect endmember assignment that is used in the model, but not actually present (Roberts et al., 1998).

The iterative Multiple Endmember Spectral Mixture Analysis (MESMA) technique can account for within-class variability and is applied by running numerous models for a pixel and selecting one model based on its ability to meet selection criteria and produce the best fit, typically a minimum RMS (Painter et al. 1998). Selection criteria include fractional constraints (minimum and maximum fraction constrains), maximum allowable blackbody fraction, RMSE constraints and a residual constraint set to remove any model that exceeds a threshold over a range of wavelengths. Using this approach, pixel-scale limits in spectral dimensionality are recognized despite the considerable spectral variability within a scene. The model constraints are variably selectable, whereby MESMA can also be run in an unconstrained mode. Previous studies have found that the flexible MESMA approach resulted in the majority of pixels in an image being modeled with only two-endmember models (Roberts et al. 1998). For example, Powell and Roberts (2008) found that natural landscapes in Brazil required only two-endmember models, disturbed regions required three- and urban areas required four-endmember models.

3.2 Wight Percent Silica (WPS)

Spectral characteristics of each mineral derive from the interaction between electromagnetic radiation and the atoms and molecules that compose it. In the TIR spectral region, the dominant features are related to the Si-O stretching vibration, which shape depends on variations in Si-O bond structure of the silicate minerals. Within this band, the emissivity minimum appears at shorter wavelengths (around 8.5 μm) for framework silicates such as quartz and feldspar and shifts progressively toward longer wavelengths in minerals with sheet, chain, or isolated tetrahedral structures (Hunt, 1980).

Building on this concept and based on the methodology presented in Hook et al., (2005), in addition to the endmember mapping, the WPS in each pixel is also included in the SM output.

The strength of Si-O bond increases due to changes in the bond configurations from minerals common in more mafic igneous rocks to those common in more felsic ones. With the increase in bond strength, the RF shifts from shorter wavelengths for felsic rocks with high WPS longer wavelengths for mafic rocks with low WPS content.

These spectral shifts can be used to not only map the endmember mineral fractions but also serve as a basis for quantifying the WPS content of different geologic surfaces using TIR remote sensing with a sufficient number of bands (at least 5). For example, past studies found that WPS content could be determined by fitting a Gaussian function to emissivity spectra to determine the wavelength position of the Gaussian minimum (Hook et al, 2005). A linear relationship between that minimum wavelength and the SiO_2 content derived from the chemical analyses of field samples was then used as the basis for the WPS algorithm.

6 Surface Mineralogy (SM) Algorithm

The surface mineralogy (SM) algorithm, developed for SBG-TIR Level-3 Surface Mineralogy product, rapidly and accurately detect mineral abundances across Earth's low vegetation surfaces (i.e., dunes, volcano, wildland fire scars, arid regions) with a low RMSE. In the early stage, two main groups of algorithms were tested: SMA (Section 3.1.1) and MESMA (Section 3.1.2), based on the widespread usage in the community and previous development and refinement activities. Given the option of using a greater number of endmembers compared to the number of wavelength that characterized the emissivity input data, the possibility to produce

mineralogical maps for each endmember plus a residual error for each pixel (emissivity spectrum) related to the specific wavelength and an overall RMS error map, the final choice was MESMA. The current endmember suite for the SM product – alias spectral library – is composed by the nine most abundant minerals on the Earth's surface, with possibility to update the suite in the future for new mineral detection.

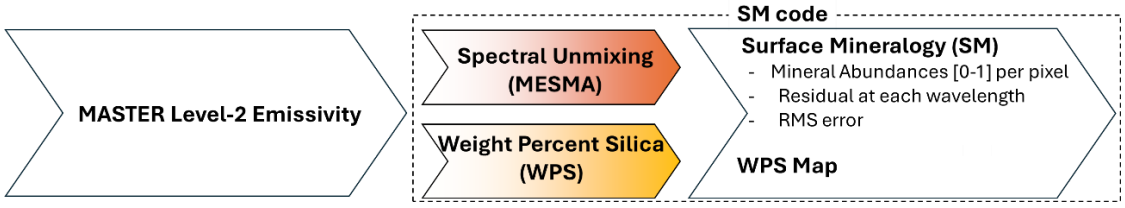

Figure 5: Workflow for the MASTER Level 3 Surface Mineralogy product from the MASTER Level 2 emissivity data.

6.1 Spectral Library Endmember Selection

For the MASTER Level 3 SM product, the spectral endmembers were chosen based on those defined for the SBG-TIR Level 3 SM product. In fact, all analyses performed for SBG-TIR regarding the testing and validation of the SM code can be applied to MASTER due to the similarity of the emissivity data.

As for SBG-TIR Level 3 SM product, nine endmembers have been selected because they are major rock-forming minerals and are generally considered the most abundant on the Earth's surface. The focus of the TIR Surface Mineralogy product is on silicate minerals (with two exceptions), all of which have dominate spectral features in the TIR region.

Table 4: Endmember minerals selected for the SM product spectral library

Mineral Name	Mineral Class	Mineral Group	Chemical Formula	ASU Spectral Library number
Andesine	silicate	feldspar	$(Ca, Na)(Al, Si)_4O_8$	434
Augite	silicate	pyroxene	$(Ca,Na)(Mg,Fe,Al,Ti)(Si,Al)_2O_6$	480
Calcite	carbonate		$CaCO_3$	527
Forsterite	silicate	olivine	Mg_2SiO_4	441
Gypsum	sulfate		$CaSO_4 \cdot 2H_2O$	758
Hornblende	silicate	amphibole	$Ca_2(Mg,Fe,Al)_5(Al,Si)_8O_{22}(OH)_2$	469
Microcline	silicate	feldspar	$KAlSi_3O_8$	490
Muscovite	silicate	mica	$KAl_2(AlSi_3O_{10})(F,OH)_2$	449
Quartz	silicate		SiO_4	1969

The spectral are plotted in Figure 6 at full spectral resolution (2 cm^{-1}) and down sampled to the MASTER TIR resolution. The addition of the tenth blackbody ($\varepsilon = 1.0$ at all wavelengths) endmember provides a way to account for the discrepancy in spectral depth between the laboratory-measured endmember minerals and that of the image-based data. A blackbody endmember image will be produced, however if normalized out of the total percentage per pixel, the remaining endmember percentages will sum to 100%.

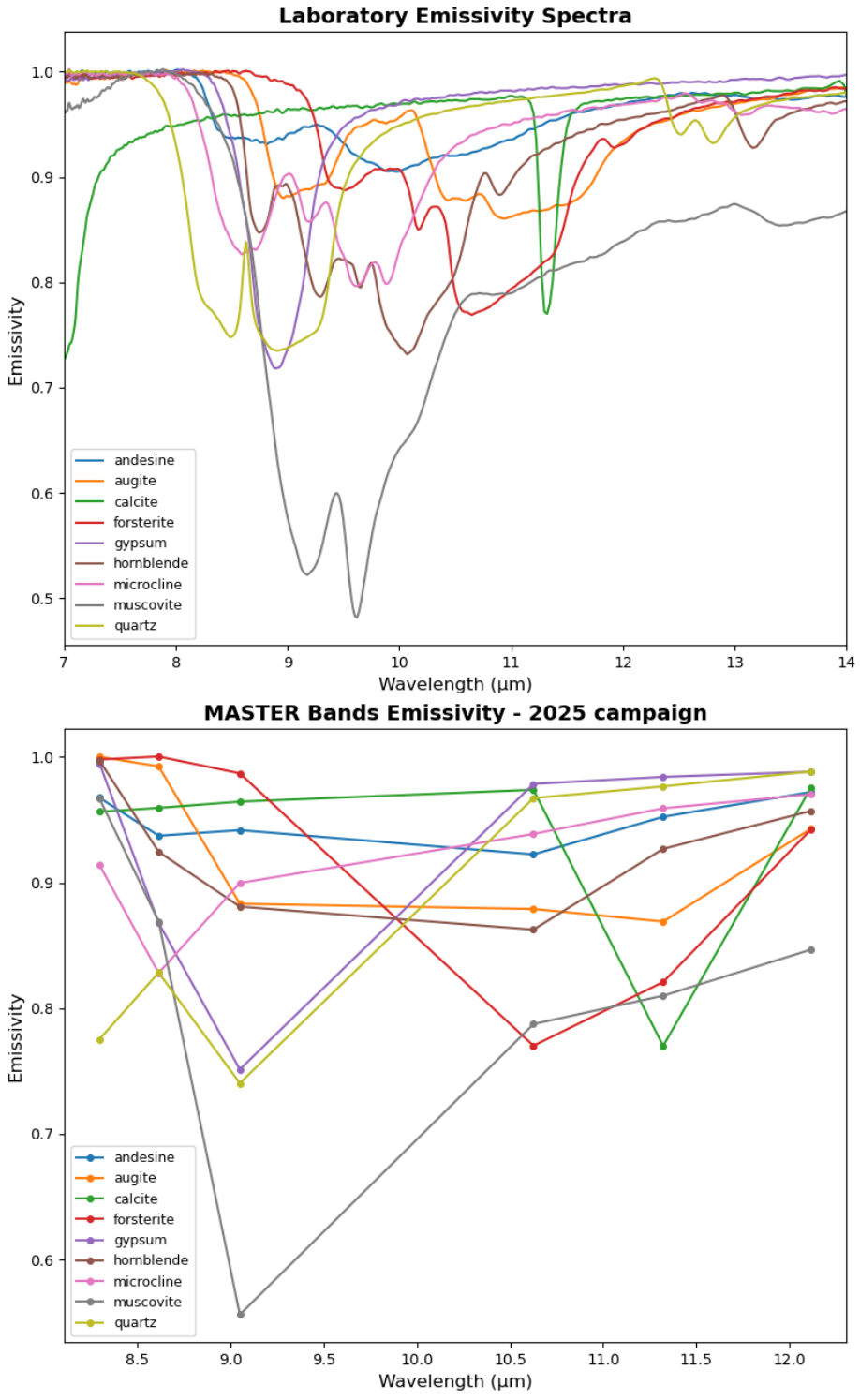

Figure 6: TIR (8.0 – 13.0 μm) spectral emissivity endmembers chosen for testing and eventual implementation of the SM Algorithm. Top: laboratory spectral resolution. Bottom: spectra resampled to the MASTER TIR spectral resolution. Data from: ASU Spectral Library (Christensen et al., 2000).

6.2 MASTER Level-3 SM output

The output of the MASTER Level-3 Surface Mineralogy product is in .hdf5 file containind the SDS "SurfaceMineralogy". The SDS contains 17 bands derived from the surface mineralogy detection. The first 9 bands represent spefific mineral aboundaces, floowew by quality metrics and error estimates for the spectral unmixing analysis and the WPS map.

Table 5: The Scientific Data Sets (SDSs) for the L3 MASTER Surface Mineralogy (SM) product

Product	SDS	Data type	Units	Valid Range	Scale Factor	Offset
SMA	*SurfaceMineralogy*	Float32	n/a	n/a	n/a	n/a
idx	**Attributes/Layers/Bands**				**Description**	
0	*andesine*	float32	n/a	[0 1]	Abundancy map for each endmember in the spectral library. This includes the blackbody to account the spectral depth difference between the reference and the actual data.	
1	*augite*	float32	n/a	[0 1]		
2	*calcite*	float32	n/a	[0 1]		
3	*forsterite*	float32	n/a	[0 1]		
4	*gypsum*	float32	n/a	[0 1]		
5	*hornblende*	float32	n/a	[0 1]		
6	*microcline*	float32	n/a	[0 1]		
7	*muscovite*	float32	n/a	[0 1]		
8	*quartz*	float32	n/a	[0 1]		
9	*blackbody*	float32	n/a	[0 1]		
10	*RMS*	float32	n/a	n/a	$\sqrt{\sum_{j=1}^{m} \delta(\lambda)_j^2 / m}$	
11	*B1 Residual Error*	float32	n/a	n/a	$\varepsilon(\lambda)_{predicted} - \varepsilon(\lambda)_{measured}$	
12	*B2 Residual Error*	float32	n/a	n/a		
13	*B3 Residual Error*	float32	n/a	n/a		
14	*B4 Residual Error*	float32	n/a	n/a		
15	*B5 Residual Error*	float32	n/a	n/a		
16	*B6 Residual Error*	float32	n/a	n/a		
17	*WPS*	float32	%	[0-100]	Whight Percent Silica	

7 Acknowledgements

The research was carried out at the Jet Propulsion Laboratory, California Institute of Technology, under a contract with the National Aeronautics and Space Administration.

8 References

Adams, J.B., Smith, M.O., Johnson, P.E. (1986). Spectral mixture modeling: A new analysis of rock and soil types at the Viking Lander 1 site. Journal of Geophysical Research: Solid Earth, 91(B8), 8098-8112.

Christensen, P.R., Bandfield, J.L., Hamilton, V.E., Howard, D.A., Lane, M.D., Piatek, J.L., ... Stefanov, W.L. (2000). A thermal emission spectral library of rock-forming minerals. Journal of Geophysical Research: Planets, 105(E4), 9735-9739.

Clark, R.N., Swayze, G.A., Wise, R., Livo, K.E., Hoefen, T.M., Kokaly, R.F., Sutley, S.J. (2003). USGS digital spectral library splib06a. US Geological Survey, Open File Report, 3395.

Connelly, D.S., Thompson, D.R., Mahowald, N.M., Li, L., Carmon, N., Okin, G.S., Green, R. O. (2021). The EMIT mission information yield for mineral dust radiative forcing. Remote Sensing of Environment, 258, 112380.

Gillespie, A. R. (1990). Interpretation of residual images: spectral mixture analysis of AVIRIS images, Owens Valley, California. In Proc. second airborne visible/infrared imaging spectrometer (AVIRIS) workshop (pp. 243-270). Jet Propulsion Laboratory.

Gillespie, A., Rokugawa, S., Matsunaga, T., Cothern, J.S., Hook, S., Kahle, A.B. (1998). A temperature and emissivity separation algorithm for Advanced Spaceborne Thermal Emission and Reflection Radiometer (ASTER) images. IEEE Transactions on Geoscience and Remote Sensing, 36, 1113-1126

Heinz, D. C. (2001). Fully constrained least squares linear spectral mixture analysis method for material quantification in hyperspectral imagery. IEEE transactions on geoscience and remote sensing, 39(3), 529-545.

Hook, S. J. Myers, J. J., Thome, K. J., Fitzgerald, M. and A. B. Kahle, 2001. The MODIS/ASTER airborne simulator (MASTER) - a new instrument for earth science studies. Remote Sensing of Environment, vol. 76, Issue 1, pp. 93-102.

Hook, S.J., Dmochowski, J.E., Howard, K.A., Rowan, L.C., Karlstrom, K.E., Stock, J. M. (2005). Mapping variations in weight percent silica measured from multispectral thermal infrared imagery—Examples from the Hiller Mountains, Nevada, USA and Tres Virgenes-La Reforma, Baja California Sur, Mexico. Remote Sensing of Environment, 95(3), 273-289.

King, M. D., Menzel, W. P., Grant, P. S., Myers, J. S., Arnold, G. T., Platnick, S. E., Gumley, L. E., Tsay, S. C., Moeller, C. C., Fitzgerald, M., Brown, K. S., & Osterwisch, F. G. (1996). Airborne scanning spectrometer for remote sensing of cloud, aerosol, water vapor and surface properties. Journal of Atmospheric and Oceanic Technology, 13, 777 ± 794.

Norman, J.M., Becker, F. (1995). Terminology in thermal infrared remote sensing of natural surfaces. Agricultural and Forest Meteorology, 77(3-4), 153-166.

Painter, T. H., Roberts, D. A., Green, R. O., & Dozier, J. (1998). The effect of grain size on spectral mixture analysis of snow-covered area from AVIRIS data. *Remote Sensing of Environment*, *65*(3), 320-332.

Powell, R.L., Roberts, D. A. (2008). Characterizing variability of the urban physical environment for a suite of cities in Rondonia, Brazil. Earth Interactions, 12(13), 1-32.

Rabuffi F., Hook S.J., Cawse-Nicholson K., Hulley G.C., Ramsey M.S., and Thompson J.O., "Estimating mineral abundances from SBG-TIR simulated data," in Proc. AGU Fall Meeting Abstr., vol. 2024, 2024, Paper GC41H–0018.

Ramsey, M.S., Christensen, P. R. (1998). Mineral abundance determination: Quantitative deconvolution of thermal emission spectra. Journal of Geophysical Research: Solid Earth, 103(B1), 577-596.

Ramsey M.S., Thompson J.O., Hulley G.C., and Rabuffi F., "Mapping the Earth's surface: Retrieving global rock-forming mineralogy with future SBG thermal infrared data," in Proc. AGU Fall Meeting Abstr., Jul. 2024, pp. 3–4

Ramsey M.S., Thompson J.O., and Rabuffi F., "Mapping global rock-forming mineralogy with future SBG thermal infrared data," in Proc. IEEE Int. Geosci. Remote Sens. Symp. (IGARSS), May 2025.

Roberts, D.A., Gardner, M., Church, R., Ustin, S., Scheer, G., Green, R. O. (1998). Mapping chaparral in the Santa Monica Mountains using multiple endmember spectral mixture models. Remote sensing of environment, 65(3), 267-279.

Sabol, D.E., Adams, J.B., Smith, M.O. (1992). Quantitative subpixel spectral detection of targets in multispectral images. Journal of Geophysical Research: Planets, 97(E2), 2659-2672.

Somers, B., Asner, G. P., Tits, L., Coppin, P. (2011). Endmember variability in spectral mixture analysis: A review. Remote Sensing of Environment, 115(7), 1603-1616. Wan, Z.M., & Dozier, J. (1996). A generalized split-window algorithm for retrieving land-surface temperature from space. Ieee Transactions on Geoscience and Remote Sensing, 34, 892-905

Tompkins, S., Mustard, J. F., Pieters, C. M., Forsyth, D. W. (1997). Optimization of endmembers for spectral mixture analysis. Remote Sensing of Environment, 59(3), 472-489.